Guided wave damage characterization via minimum variance imaging with a distributed array of ultrasonic sensors

James S. Hall[(a)], Paul Fromme[(b)], and Jennifer E. Michaels[(c)†]

[(a)] Hidden Solutions, LLC, Kissimmee, FL

[(b)] Department of Mechanical Engineering, University College London, London, UK

[(c)] School of Electrical and Computer Engineering, Georgia Institute of Technology, Atlanta, GA, USA 30332-0250

ABSTRACT. Guided wave imaging with a distributed array of inexpensive transducers offers a fast and cost-efficient means for damage detection and localization in plate-like structures such as aircraft and spacecraft skins. As such, this technology is a natural choice for inclusion in condition-based maintenance and integrated structural health management programs. One of the implementation challenges results from the complex interaction of propagating ultrasonic waves with both the interrogation structure and potential defects or damage. For example, a guided ultrasonic wave interacts with a surface or sub-surface defect differently depending on the angle of incidence, defect size and orientation, excitation frequency, and guided wave mode. However, this complex interaction also provides a mechanism for guided wave imaging algorithms to perform damage characterization in addition to damage detection and localization. Damage characterization provides a mechanism to help discriminate actual damage (e.g. fatigue cracks) from benign changes, and can be used with crack propagation models to estimate remaining life. This work proposes the use of minimum variance imaging to perform damage detection, localization, and *characterization*. Scattering assumptions used to perform damage characterization are obtained through both analytical and finite element models. Experimental data from an *in situ* distributed array are used to demonstrate feasibility of this approach using a through-hole and two through-thickness notches of different orientations to simulate damage in an aluminum plate.

Keywords: Lamb waves; structural health monitoring; nondestructive evaluation; minimum variance; MVDR; scattering

[†]Electronic mail: jemichaels@gatech.edu

I. INTRODUCTION

Ultrasonic guided waves are capable of quickly interrogating large plate-like structures and are sensitive to both surface and subsurface features [1]. As such, significant efforts have recently been expended to use them for damage detection and localization in structures such as aircraft skins [2]. Since inexpensive piezoelectric transducers can both generate and receive guided waves with reasonable mode selectivity and omnidirectional sensitivity [3], permanently attached distributed arrays of these transducers offer a cost-effective *in situ* structural health monitoring (SHM) solution for both aging aircraft and new aerospace designs. Since *in situ* monitoring does not require the system to be taken out-of-service for inspection, the cost of measurements can be reduced compared to current NDE methods and measurements can be performed much more frequently, which potentially decreases the inspection cost of condition-based obsolescence schedules and increases safety margins.

To date, distributed arrays of piezoelectric transducers have already been demonstrated to be capable of detecting and locating damage [4]. Unlike conventional ultrasonic NDE methods, which directly interpret signals without comparisons to baseline data, damage detection using *in situ* piezoelectric sensors is typically performed by recording baseline signals during a known good condition and comparing them to signals recorded after some service period. If the difference between signals exceeds a predetermined threshold, then the interrogation system indicates that damage may be present. Damage localization is performed with the same differenced signals through guided wave imaging techniques. Several guided wave imaging methods are in use, including tomographic [5], maximum-likelihood [6], sparse reconstruction [7], and elliptical imaging algorithms [4, 8, 9]. These imaging methods all produce an intensity map that corresponds to the interrogation structure, with the brightest pixels indicating the most

likely damage location(s). It is advantageous to image with differenced signals (i.e., after baseline subtraction) to separate scattered echoes from both incident waves and geometrical reflections (e.g., from boundaries). This separation is typically done by time windowing for bulk wave phased array imaging; such windowing is generally not possible for sparse guided wave signals.

In addition to damage localization, elliptical guided wave imaging algorithms also offer the potential to perform damage characterization. The geometric structure of a damage site or defect, such as size, orientation, etc., has a profound impact on the scattering behavior. Significant efforts have been conducted to characterize and experimentally validate the scattering behavior of guided waves for complete and partial through-thickness holes [10-14], notches [15, 16], and cracks [17, 18]. Since guided wave imaging algorithms have the ability to incorporate the anticipated scattering behavior of potential defects, these imaging algorithms can be used to distinguish between defect types. This approach is similar to that used by Zhang *et al.* [19], which characterizes the scattering field of potential defects using bulk waves.

This paper proposes the use of minimum variance imaging [9] for not only damage localization but also damage characterization, and is a continuation of the work presented in [20]. Minimum variance imaging is an elliptical imaging algorithm that minimizes imaging artifacts while maintaining sensitivity to damage by adaptively computing the signal weighting coefficients. Damage characterization is performed by generating minimum variance images for various scattering assumptions and determining which image contains the strongest response at the potential damage location. The scattering assumption that produces this response is then assumed to correspond to the underlying defect or damage. The primary contribution of this

paper is a methodology that uses adaptive imaging in combination with a library of scattering patterns to achieve *in situ* damage characterization.

This paper is organized as follows. Elliptical guided wave imaging and its use for damage localization and characterization is discussed in Section II. Section III describes the experimental setup and testing procedure and Section IV provides details about the methods used to calculate the scattered wave fields. Experimental results and their analysis are presented in Section V, which is followed by the conclusions.

II. ELLIPTICAL IMAGING

This section provides a brief introduction to elliptical guided wave imaging, including both conventional delay-and-sum imaging as well as minimum variance imaging. The reader is referred to [9] and [21] for a more in depth discussion, including a formal derivation of the algorithm and implementation details.

When performing guided wave imaging for structural health monitoring, differenced signals are typically used. Differenced signals are obtained by subtracting a known good, or baseline signal, from the test signal. This operation, referred to as baseline subtraction, isolates any changes between the two signals. For guided wave imaging to produce meaningful results, it is important that any differences between these two signals correspond to scattering from defects or damage. In reality, however, there are a number of factors that can produce significant changes in the signals that are unrelated to damage, including changes in temperature, surface conditions, and applied loads [22-25]. If uncompensated, the imaging artifacts that result from these factors can both mask legitimate damage and cause false positives.

Elliptical imaging is performed by computing each pixel directly from the differenced signals. To begin, consider an excitation function that is centered at time $t = 0$. If damage is

present at pixel location (x,y), then each differenced signal should contain some scattered energy at time τ, defined as:

$$\tau_{ixy} = \frac{d_{ixy}}{c_g}, \tag{0}$$

where i indicates a specific transducer pair, xy identifies the (x,y) coordinate, d_{ixy} is the total propagation distance from transmitter to pixel location (x,y) to receiver for the ith transducer pair, and c_g is the group velocity. The group velocity corresponding to the center excitation frequency is employed to calculate the arrival time of the center of the wave packet. Dispersion leads to the spreading of the wave packet but not to a change in the arrival time of the pulse center (maximum amplitude). Since the differenced signal from the ith transducer pair contains scattered energy at time τ_{ixy}, then the pixel intensity, P_{xy}, is non-zero when damage is present:

$$P_{xy} = \sum_{i=1}^{N} \left| w_{ixy} r_i \left(\tau_{ixy} \right) \right|^2, \tag{0}$$

where $r_i(t)$ is the differenced signal for the ith transducer pair and w_{ixy} is a weighting coefficient that is specific to both transducer pair and pixel location. It should be noted here that the above equation is sometimes presented using an additional integration over a predetermined time-window. It was shown in [9], however, that imaging performance is improved by reducing the integration window to an instantaneous point in time. For simplicity, the above equation can be rewritten in matrix format:

$$P_{xy} = \vec{\mathbf{w}}_{xy}^{\mathrm{H}} \mathbf{R}_{xy} \vec{\mathbf{w}}_{xy}, \tag{0}$$

where "H" indicates a Hermetian transpose operation, $\vec{\mathbf{w}}_{xy}$ is a vector of weighting coefficients, and $\mathbf{R}_{xy}$ is a singular autocorrelation matrix defined as $\mathbf{R}_{xy} = \vec{\mathbf{r}}_{xy} \vec{\mathbf{r}}_{xy}^{\mathrm{H}}$. The measurement vectors, $\vec{\mathbf{r}}_{xy}$, used to define $\mathbf{R}_{xy}$ are composed of the $r_i \left(\tau_{ixy} \right)$ values from Eq. (2).

The choice of weighting coefficients, $\vec{\mathbf{w}}_{xy}$, plays a fundamental role in imaging performance. As implemented here, the weighting coefficients for delay-and-sum elliptical imaging, referred to as conventional imaging throughout this paper, are scaled to produce a unit vector that maximizes the pixel value, P_{xy}, *if damage is present*. When damage is present, each element of the measurement vector, $\vec{\mathbf{r}}_{xy}$, is related to the others as:

$$\begin{aligned}\vec{\mathbf{r}}_{xy} &= \left[r_1\left(\tau_{1xy}\right) \quad \cdots \quad r_N\left(\tau_{Nxy}\right) \right]^{\mathrm{T}} \\ &= x_0 \left[\frac{\psi_{1xy}}{\sqrt{d^{\times}_{1xy}}} \quad \cdots \quad \frac{\psi_{Nxy}}{\sqrt{d^{\times}_{Nxy}}} \right]^{\mathrm{T}},\end{aligned} \tag{0}$$

where x_0 is the excitation signal evaluated at time $t = 0$, $d^{\times}_{ixy}$ is the propagation distance from transmitter to pixel location (x,y) *multiplied by* the propagation distance from pixel location (x,y) to receiver for the ith transducer pair, and ψ_{ixy} corresponds to the scattering behavior of the damage or defect at pixel location (x,y) for the ith transducer pair. Note that the multiplication of propagation distances in $d^{\times}_{ixy}$ is appropriate for the assumption that the damage acts as a point source in the far field since geometric loss occurs in two distinct stages. Since $\vec{\mathbf{w}}_{xy}$ is constrained to be a unit vector, the pixel value, P_{xy} defined in Eq. (3), will be maximized when $\vec{\mathbf{w}}_{xy}$ is proportional to $\vec{\mathbf{r}}_{xy}$, as defined in Eq. (4), and therefore the weighting vector for conventional imaging is defined as:

$$\vec{\mathbf{w}}_{\mathrm{CV}} \propto \left[\frac{\psi_{1xy}}{\sqrt{d^{\times}_{1xy}}} \quad \cdots \quad \frac{\psi_{Nxy}}{\sqrt{d^{\times}_{Nxy}}} \right]^{\mathrm{T}}. \tag{0}$$

Conventional imaging has been shown to be capable of performing reasonably well, even in the absence of *a priori* information about potential scatterers (i.e., ψ_{ixy} is not known and is therefore assigned an arbitrary constant value). However, it is susceptible to significant imaging artifacts

that can mask the presence of damage or cause false positives. As such, Minimum Variance Distortionless Response (MVDR) has been incorporated into the algorithm to reduce imaging artifacts and improve imaging resolution [9]. In addition to maximizing the pixel value when damage is present, as is the case for conventional imaging, minimum variance imaging also attempts to *minimize* the pixel value when damage is absent. Rather than defining the weighting vectors as in Eq. (5), the weighting vectors in minimum variance imaging are chosen to satisfy the following constrained optimization problem:

$$P_{xy} = \min_{\vec{\mathbf{w}}} \vec{\mathbf{w}}^{\mathrm{H}} \mathbf{R}_{xy} \vec{\mathbf{w}}, \quad \text{such that} \quad \vec{\mathbf{w}}^{\mathrm{H}} \vec{\mathbf{e}}_{xy} = 1, \tag{0}$$

where $\vec{\mathbf{e}}_{xy}$ is a unit norm vector referred to as the "steering vector" and is equal to $\vec{\mathbf{w}}_{\mathrm{CV}}$ for conventional imaging. In effect, minimum variance imaging will minimize *all* pixel values throughout the image, subject to the constraint that $\vec{\mathbf{w}}^{\mathrm{H}} \vec{\mathbf{e}}_{xy} = 1$, which ensures that the pixel value at a damage location is *not* minimized since $\vec{\mathbf{e}}_{xy} = \vec{\mathbf{w}}_{\mathrm{CV}}$ with $\vec{\mathbf{w}}_{\mathrm{CV}}$ defined in Eq. (5).

The constrained optimization problem can be solved through the use of a Lagrange multiplier. The value of $\vec{\mathbf{w}}$ that satisfies Eq. (6) is:

$$\vec{\mathbf{w}}_{MV} = \frac{\mathbf{R}_{xy}^{-1} \vec{\mathbf{e}}_{xy}}{\vec{\mathbf{e}}_{xy}^{\mathrm{H}} \mathbf{R}_{xy}^{-1} \vec{\mathbf{e}}_{xy}}, \tag{0}$$

where the "−1" superscript indicates a matrix inverse. Since $\mathbf{R}_{xy}$ is known to be a singular matrix, the inversion process is regularized through diagonal loading. For all imaging presented in this paper, the weight of the diagonal loading is 0.1 times the squared magnitude of $\vec{\mathbf{r}}_{xy}$. It should be noted that additional optimizations exist to reduce computation time; for the cases considered in this paper, minimum variance imaging can be computed without performing a complete matrix inversion, which allows the imaging process to complete in a comparable

amount of time as conventional imaging. Details about implementation optimizations can be found in [21].

III. EXPERIMENTAL SETUP AND PROCEDURE

The experimental setup is illustrated in Fig. 1. Six piezoelectric transducers were attached in a randomized pattern to a 914 mm × 914 mm × 3.18 mm 6061 aluminum plate to simulate the interrogation of a large plate-like structure for damage. The transducers were 300 kHz, radial mode PZT disks, 7 mm in diameter and 0.5 mm thick, and were attached to the plate using two-part epoxy. They were backed with a bubble-filled epoxy layer for mechanical protection and also to strain-relieve the soldered wire connections. Although realistic structures are likely to have more complex geometries, the setup employed here is intended to provide a proof-of-concept, allowing damage characterization to be demonstrated without the additional complications introduced by a more complex structure.

The plate was interrogated with a 10-cycle Hann-windowed sinusoid with a center frequency of 300 kHz. The frequency was selected because it was experimentally found to maximize the energy ratio of S_0 to A_0 and is below the cutoff frequency of higher-order modes. Although the SH_0 mode was also present in the recorded data, the amplitude was negligible compared to both S_0 and A_0. At these frequencies, the S_0 mode is highly dispersive, meaning that the phase velocity of the guided wave varies with frequency. Therefore, a narrow-bandwidth tone burst was used to minimize spreading of the wave packet in time due to dispersion. Another means of minimizing the effects of dispersion would be to apply dispersion compensation [26], but this approach requires accurate knowledge of the dispersion curves, which may not always be available.

A dataset is composed of signals from each unique transducer pair obtained in a round-robin fashion (1→2, 1→3, ... , 5→6). For the six-transducer array considered here, this produces 15 recorded signals. Reciprocal signals (2→1, 3→1, etc.) were not recorded in the interest of time since they do not contain additional information.

The experiment was conducted as follows. First, a dataset was recorded under known good conditions with no simulated damage present. A 5 mm diameter through-hole was drilled in the top-left corner, labeled "Hole" in Fig. 1(b), and a second set of signals was recorded. A 15 mm × 2 mm through thickness notch oriented 45° from horizontal was then introduced in the bottom-right corner of the plate, labeled "+45° Notch" in Fig. 1(b); a third set of data was then recorded. At that point, a second 15 mm × 2 mm through thickness notch oriented −45° from horizontal was introduced at the site labeled "−45° Notch" in Fig. 1(b). A fourth and final set of data was then obtained, completing the experimental data acquisition. Note that both notches were hand-cut and had slight irregularities on the edges, and all four datasets were recorded at nominally the same temperature. Table 1 summarizes the transducer locations and the nominal defect locations. Figure 2 shows signals from transducer pair 3-5 before and after drilling of the through-hole along with the residual (differenced) signal after baseline subtraction. The first arrival pulse (~ 65-100 μs) corresponds to the S_0 mode directly propagating between the two transducers and is almost identical between the baseline and defect signal. The later pulses in the baseline signal correspond to reflections at the plate edges, which typically overlap in time, as well as the slower and much lower amplitude A_0 mode. The first significant difference between the signals at about 150 μs corresponds to the wave pulse scattered at the hole and received at transducer #5. Further reflections at the plate edges of the scattered wave can be observed in the differenced signal later than 200 μs.

To improve baseline subtraction results, a slight phase shift was applied to the baseline signals to better match the test data. The non-ideal baseline subtraction was likely caused by small temperature variations in the laboratory (not measured) combined with timing jitter due to the fairly coarse sampling frequency of 12.5 MHz. The phase shift was chosen to minimize the baseline subtraction residual either over the entire recording or over the direct-arrival to improve the resulting image quality. Although such an approach is less than ideal, the proposed method for damage characterization is predicated on successful baseline subtraction, which is a distinctly separate problem from damage characterization and is an area of ongoing research [22-25].

IV. SCATTERING BEHAVIOR

For minimum variance imaging to perform damage characterization, the steering vector, $\vec{\mathbf{e}}_{xy}$, used to calculate the pixel value must correspond to the measurement vector, $\vec{\mathbf{r}}_{xy}$. Since the steering vectors are largely defined by the scattering coefficients, ψ_{ixy}, accurate knowledge of scattering coefficients is necessary to maximize imaging performance. Scattering coefficients were estimated differently depending on the damage type, using an analytic model for the through-hole and finite element modeling (FEM) for the notches. In both cases, nominal aluminum 6061 material properties were assumed.

For the 5 mm diameter through-hole, scattering behavior was estimated using the approach derived by Grahn [14] for 300 kHz S_0 incident and scattered waves. This low frequency approximation is a computationally efficient method for obtaining scattering coefficients and is capable of accounting for partial through-thickness holes in addition to the through-thickness model used here.

Three dimensional FEM simulations with the ABAQUS software suite were performed to generate scattering fields for a through-thickness notch (2 mm × 15 mm) in a large aluminum

plate (thickness of 3.18 mm, size of 800 mm × 800 mm). Each FEM simulation used explicit time integration, with linear brick elements of 1.25 mm in the direction along the notch, 1 mm in the direction of the notch thickness, and 0.795 mm through the plate thickness. Excitation of the S_0 mode was performed using opposing out-of-plane point-sources located 300 mm from the defect location at the top and bottom edges of the plate with a 10-cycle Hann-windowed tone burst at 300 kHz. Out-of-plane time traces were obtained from one surface of the plate on a 49 mm × 61.25 mm grid centered at the notch. Since both the excitation and the notch are symmetric about the center of the plate, the recorded data contained only the S_0 mode. As the scattering characteristics of notches depend strongly on the orientation of the defect relative to the incident wave field, the FEM simulations were repeated for incident waves over a 90° range relative to the notch orientation using 5° increments. The symmetries of a notch allow the scattering behavior for the remaining incident angles to be inferred from these simulations.

Scattering behavior was obtained from the FEM simulations using the same baseline subtraction technique as used for guided wave imaging described in Section II. A complete FEM simulation was first performed without a notch and then repeated with the notch. Data from the two simulations were then differenced in the time domain to isolate the effects of the notch. Differenced information from the rectangular grid was spatially interpolated to obtain measurements located at 1° increments along a circle of radius 24 mm centered at the notch location. Each of these 359 signals was then converted to the frequency domain and the magnitude and phase at 300 kHz were used to determine the scattering behavior. All scattering behavior estimates were normalized in terms of both magnitude and phase relative to a direct arrival that propagated the same distance.

Figure 3 shows the S_0 scattering behavior obtained from FEM simulations for a 15 mm × 2 mm through thickness notch for an incident S_0 wave. Figure 3(a) depicts the magnitude of the *differenced* (i.e., scattered) signal as a function of both incident and scattered angle for *all* angles. For example, the diagonal high amplitude region in the center of the figure (around incident and scattered angles of 0°) corresponds to forward scattering for broadside incidence where the incident and scattered angle are approximately the same. The diagonal region of high scattered amplitude at the bottom (and top) of the figure corresponds to backscattering for broadside incidence (i.e., an incident angle of 0° and a scattered angle of ±180°). It can also be seen that for end-on incidence (i.e., incident angles of ±90°) the amplitude of the scattered wave is significantly lower with slightly more forward scattering than backscattering. Figure 3(b) illustrates the same information for incident angles of 0°, −45°, and −90° displayed as a polar plot. The color-coded arrows depict the incident wave propagation directions. These figures show that for the 0° incident wave, the signal is largely reflected back towards the source, producing two large lobes. The lobe in the forward (0°) direction corresponds to the *lack* of signal that will be evident in the differenced signal due to the "shadowing"" effect of the notch, while the lobe in the backward (−180°) direction corresponds to the reflected wave. For an incident angle of −45°, a slightly smaller lobe in the forward direction can again be observed due to the blocking of the wave propagation. However, less reflected wave amplitude can be observed for the oblique incident wave from the two small lobes. For the incident wave propagating along the defect orientation (−90°), a significantly smaller scattering effect can be observed with a small part of the wave energy blocked and very limited backscattering. Figure 3 highlights the directionally dependent nature of the scatterer, with dependencies on both the incident and scattered angles.

It is important to note that the unit-norm steering vector described in Eq. (5) is a function of the *relative* scattering behavior between different incident and reflected angle combinations. Since the vector is normalized to have unit-norm, two scatterers that differ only by a constant scale factor will produce identical images. As such, the overall normalization of scattering behavior for a particular defect has no effect on imaging performance as long as the scattering behavior is self-consistent. This phenomenon also facilitates the comparison between scattering behavior estimated through separate methods, as is the case here with the through-hole and notch scattering estimates.

V. EXPERIMENTAL RESULTS

Experimental data were collected as described in Section III. Rather than using damage-free baseline data for baseline subtraction, however, baseline signals were chosen to be the data collected just prior to the introduction of each simulated defect. This selection of baselines isolates the energy from one scatterer without the complications of scattering from multiple defects. In the interest of simplicity, the envelope of the time domain differenced signals is used for all imaging.

Figure 4 illustrates conventional imaging results for the +45° notch. The plots correspond to the scattering behavior used for imaging: (a) a 5 mm diameter through-hole (based on [14]); (b) a 15 mm × 2 mm through-thickness notch oriented +45° from horizontal (based on FEM simulations); and (c) a 15 mm × 2 mm through-thickness notch oriented −45° from horizontal (based on FEM simulations). For comparison, the images are shown on a dB scale normalized to the overall peak pixel value of the three images. Figure 4 demonstrates that although the imaging results are somewhat improved when the scattering assumptions match the

physical defect (Fig. 4b), the large imaging artifacts result in significant ambiguity as to both the defect location as well as type.

Figure 5 illustrates damage characterization results using minimum variance imaging and *the same data and assumptions* as used for Fig 4. The number and magnitude of imaging artifacts have been significantly reduced as compared to Fig 4. As a result, minimum variance imaging allows both the location *and type* of this defect to be clearly identified.

To compare results for all three damage types, minimum variance imaging was performed for the three data sets using all three scattering matrices (for a total of nine images). For each damage type, the image amplitudes were normalized to the overall maximum pixel in the three images, as was done in Figs. 4 and 5 for the +45° notch. Table 2 summarizes the results for both a circular region (25 mm radius) centered at the actual defect location as well as for the overall plate. For all three defects, the largest amplitude was found when the correct scattering matrix was used. The algorithm also gave the correct location; i.e., the largest amplitude was found within 25 mm of the actual defect location. Thus, minimum variance imaging was able to not only locate the defect but to also characterize it in terms of identifying the best match from a predefined set of scatterers. The most ambiguous characterization was that of the −45° notch; using the hole scattering matrix yielded amplitudes only 4 to 5 dB lower than obtained using the correct scattering matrix. This notch, which was located in the approximate center of the transducer polygon, did exhibit some apparent omnidirectional scattering, most likely caused by a combination of imperfect baseline subtraction and irregularities on the notch edges. With the exception of this worst-case situation, the margin increases to over 9 dB in the regions within 25 mm of the nominal defect locations. When considering the entire plate, there is at least a 3.3 dB margin for all three defects in terms of identifying the actual defect type.

It is of interest to note that for both notch cases, images generated using scattering assumptions corresponding to a 5 mm diameter through-hole produce higher amplitude values than those of the incorrectly rotated notch. This behavior makes intuitive sense since the directional scattering pattern of a specific notch orientation is more similar to that of a through-hole than to that of an identical notch rotated by 90°.

To further demonstrate damage characterization potential, consider the problem of determining defect *orientation,* an important parameter for remaining structural life predictions based on stress and fatigue calculations. Figure 6 depicts the pixel value at the nominal defect location for minimum variance images generated with scattering assumptions corresponding to notch orientations spanning from −90° to +90° in 1° intervals. From Fig. 6, the maximum pixel value is obtained when a notch of +43° is assumed for the +45° notch and when a notch of −47° is assumed for the −45° notch. Taking into consideration possible sources of error, e.g., imperfect baseline subtraction, dispersive effects, errors in scattering assumptions, and machining accuracy, these results demonstrate the potential of this methodology for providing good estimates of defect orientation.

These experimental results demonstrate that minimum variance imaging with a distributed array of transducers *is* capable of at least some degree of characterization of simulated damage. The approach described here for classifying the defect type as well as discerning notch orientation may also be able to successfully characterize other damage features, such as type, size, depth, and shape, and also points to the need to obtain scattering matrices for more scatterers of interest, either experimentally or via modeling.

VI. CONCLUSION

The ability to perform characterization of scatterers using minimum variance imaging with a library of known scattering matrices has been demonstrated with experimental data for both a 5 mm diameter through-hole and two 15 mm notches of different orientations located both inside and outside the transducer array polygon. The scatterers were characterized as to type (hole vs. notch) and orientation (for the notches). Although these results are limited in scope, they show the potential for at least some degree of *in situ* characterization using a spatially distributed array, which significantly increases the usefulness of guided wave SHM. The most significant application of the proposed method may be to discriminate defects, which are typically directional scatterers, from benign scatterers such as water droplets and other boundary condition changes that may not exhibit strong directionality.

VII. ACKNOWLEDGEMENTS

This work was supported by the NASA Graduate Student Research Program, Grant No. NNX08AY93H (first author), and the Air Force Office of Scientific Research, Grant No. FA9550-08-1-0241 (third author).

Table 1. Locations of the six transducers and three defects relative to the lower left corner of the plate.

Description	X (mm)	Y (mm)
Transducer #1	254	221
Transducer #2	498	150
Transducer #3	679	465
Transducer #4	687	729
Transducer #5	401	723
Transducer #6	224	455
Hole	162	744
+45° Notch	780	139
−45° Notch	507	533

Table 2. Minimum variance imaging peak amplitudes in dB for the three defects in both the defect region (25 mm radius circle) and the entire plate.

Defect Type	Hole Scattering Matrix		+45° Scattering Matrix		−45° Scattering Matrix	
	Region	Plate	Region	Plate	Region	Plate
Hole	0	0	−9.6	−3.3	−9.7	−4.6
+45° Notch	−12.4	−9.0	0	0	−19.2	−11.7
−45° Notch	−5.0	−4.6	−17.9	−11.8	0	0

REFERENCES

1. J. L. Rose, "A baseline and vision of ultrasonic guided wave inspection potential," *J. Pressure Vessel Technol.*, vol. 124, no. 3, pp. 273–282, 2002. [Online]. Available: http://dx.doi.org/10.1115/1.1491272

2. X. Zhao, H. Gao, G. Zhang, B. Ayhan, F. Yan, C. Kwan, and J. L. Rose, "Active health monitoring of an aircraft wing with embedded piezoelectric sensor/actuator netork: I. Defect detection, localization, and growth monitoring," *Smart Mater. Struct.*, vol. 16, no. 4, pp. 1208–1217, 2007. [Online]. Available: http://dx.doi.org/10.1088/0964-1726/16/4/032

3. L. Y. Yu and V. Giurgiutiu, "Piezoelectric wafer active sensors in Lamb wave-based structural health monitoring," *Journal of the Minerals, Metals & Materials Society*, vol. 64, no. 7, pp. 814-822, 2012. [Online]. Available: http://dx.doi.org/10.1007/s11837-012-0362-9

4. J. E. Michaels, "Detection, localization and characterization of damage in plates with an in situ array of spatially distributed sensors," *Smart Mater. Struct.*, vol. 17, no. 3, p. 035035, 2008. [Online]. Available: http://dx.doi.org/10.1088/0964-1726/17/3/035035

5. K. E. Leonard, E. V. Malyarenko, and M. K. Hinders, "Ultrasonic Lamb wave tomography," *Inverse Prob.*, vol. 18, no. 6, pp. 1795–1808, 2002. [Online]. Available: http://dx.doi.org/10.1088/0266-5611/18/6/322

6. E. B. Flynn, M. D. Todd, P. D. Wilcox, B. W. Drinkwater, and A. J. Croxford, "Maximum-likelihood estimation of damage localization in guided-wave structural health monitoring," *Proc. Royal Soc. A*, vol. 467, no. 2133, pp. 2575–2596, 2011. [Online]. Available: http://dx.doi.org/10.1098/rspa.2011.0095

7. R. M. Levine and J. E. Michaels, “Model-based imaging of damage with Lamb waves via sparse reconstruction,” *J. Acoust. Soc. Am.*, vol. 133, no. 3, pp. 1525-1534, 2013. [Online]. Available: http://dx.doi.org/10.1121/1.4788984

8. C. H. Wang, J. T. Rose, and F.-K. Chang, “A synthetic time-reversal imaging method for structural health monitoring,” *Smart Mater. Struct.*, vol. 13, no. 2, pp. 415–423, 2004. [Online]. Available: http://dx.doi.org/10.1088/0964-1726/13/2/020

9. J. S. Hall and J. E. Michaels, “Minimum variance ultrasonic imaging applied to an in situ sparse guided wave array,” *IEEE Trans. Ultrason., Ferroelectr., Freq. Control*, vol. 57, no. 10, pp. 2311–2323, 2010. [Online]. Available: http://dx.doi.org/10.1109/TUFFC.2010.1692

10. J. C. P. McKeon and M. K. Hinders, “Lamb wave scattering from a through hole,” *J. Sound and Vib.*, vol. 224, no. 5, pp. 843–862, 1999. [Online]. Available: http://dx.doi.org/10.1006/jsvi.1999.2164

11. P. Fromme and M. B. Sayir, “Measurement of the scattering of a Lamb wave at a through hole in a plate,” *J. Acoust. Soc. Am.*, vol. 111, no. 3, pp. 1165–1170, 2002. [Online]. Available: http://dx.doi.org/10.1121/1.1448338

12. O. Diligent, T. Grahn, A. Bostrom, P. Cawley, and M. J. S. Lowe, “The low-frequency reflection and scattering of the S0 Lamb mode from a circular through-thickness hole in a plate: finite element, analytical and experimental studies,” *J. Acoust. Soc. Am.*, vol. 111, no. 1, pp. 64–74, 2002. [Online]. Available: http://dx.doi.org/10.1121/1.1512292

13. C. H. Wang and F.-K. Chang, “Scattering of plate waves by a cylindrical inhomogeneity,” *J. Sound and Vib.*, vol. 282, no. 1-2, pp. 429–451, 2005. [Online]. Available: http://dx.doi.org/10.1016/j.jsv.2004.02.023

14. T. Grahn, “Lamb wave scattering from a circular partly through-thickness hole in a plate,” *Wave Motion*, vol. 37, no. 1, pp. 63–80, 2003. [Online]. Available: http://dx.doi.org/10.1016/S0165-2125(02)00051-3

15. M. J. S. Lowe and O. Diligent, “Low-frequency reflection characteristics of the S0 Lamb wave from a rectangular notch in a plate,” *J. Acoust. Soc. Am.*, vol. 111, no. 1, pp. 64–74, 2002. [Online]. Available: http://dx.doi.org/10.1121/1.1424866

16. P. Fromme and C. Rouge, “Directivity of guided ultrasonic wave scattering at notches and cracks,” *J. Phys.: Conf. Ser*, vol. 269, pp. 012018, 2011. [Online]. Available: http://dx.doi.org/10.1088/1742-6596/269/1/012018

17. Z. Chang and A. Mal, “Scattering of Lamb waves from a rivet hole with edge cracks,” *Mech. Mater.*, vol. 31, no. 3, pp. 197–204, 1999. [Online]. Available: http://dx.doi.org/10.1016/S0167-6636(98)00060-X

18. P. Fromme and M. B. Sayir, “Detection of cracks at rivet holes using guided waves,” *Ultrasonics*, vol. 40, no. 1-8, pp. 199–203, 2002. [Online]. Available: http://dx.doi.org/10.1016/S0041-624X(02)00137-3

19. J. Zhang, B. W. Drinkwater, and P. D. Wilcox, “Defect characterization using an ultrasonic array to measure the scattering coefficient matrix,” *IEEE Trans. Ultrason., Ferroelectr., Freq. Control*, vol. 55, no. 10, pp. 2254–2265, 2008. [Online]. Available: http://dx.doi.org/10.1109/TUFFC.924

20. J. S. Hall, P. Fromme, and J. E. Michaels, “Ultrasonic guided wave imaging for damage characterization,” in *Aircraft Airworthiness and Sustainment Conference*, 2011. [Online].

Available: http://www.meetingdata.utcdayton.com/agenda/airworthiness/2011/proceedings/techpapers/TP4562.pdf

21. J. S. Hall and J. E. Michaels, "Computational efficiency of ultrasonic guided wave imaging algorithms," *IEEE Trans. Ultrason., Ferroelectr., Freq. Control*, vol. 58, no. 1, pp. 244–248, 2011. [Online]. Available: http://dx.doi.org/10.1109/TUFFC.2011.1792

22. G. Konstantinidis, P. D. Wilcox, and B. W. Drinkwater, "The temperature stability of guided wave structural health monitoring systems," *Smart Mater. Struct.*, vol. 15, no. 4, pp. 967-976, 2006. [Online]. Available: http://dx.doi.org/10.1088/0964-1726/15/4/010

23. A. J. Croxford, J. Moll, P. D. Wilcox, and J. E. Michaels, "Efficient temperature compensation strategies for guided wave structural health monitoring," *Ultrasonics*, vol. 50, no. 4-5, pp. 517–528, 2010. [Online]. Available: http://dx.doi.org/10.1016/j.ultras.2009.11.002

24. Y. Lu and J. E. Michaels, "Feature extraction and sensor fusion for ultrasonic structural health monitoring under changing environmental conditions," *IEEE Sens. J.* , vol. 9, no. 11, pp. 1462-1471, 2009. [Online]. Available: http://dx.doi.org/10.1109/JSEN.2009.2019339

25. X. Chen, J. E. Michaels, S. J. Lee, and T. E. Michaels, "Load-differential imaging for detection and localization of fatigue cracks using Lamb waves," *NDT&E Int.*, vol. 51, pp. 142-149, 2012. [Online]. Available: http://dx.doi.org/10.1016/j.ndteint.2012.05.006

26. P. D. Wilcox, "A rapid signal processing technique to remove the effects of dispersion from guided wave signals," *IEEE Trans. Ultrason., Ferroelectr., Freq. Control*, vol. 50, no. 4, pp. 419-417, 2003. [Online]. Available: http://dx.doi.org/10.1109/TUFFC.2003.1197965

List of Figures

Figure 6. Pixel values of minimum variance images at nominal defect locations shown as a function of assumed notch orientation for 15 mm × 2 mm through thickness notches oriented at +45° and −45°.

Figure 1A

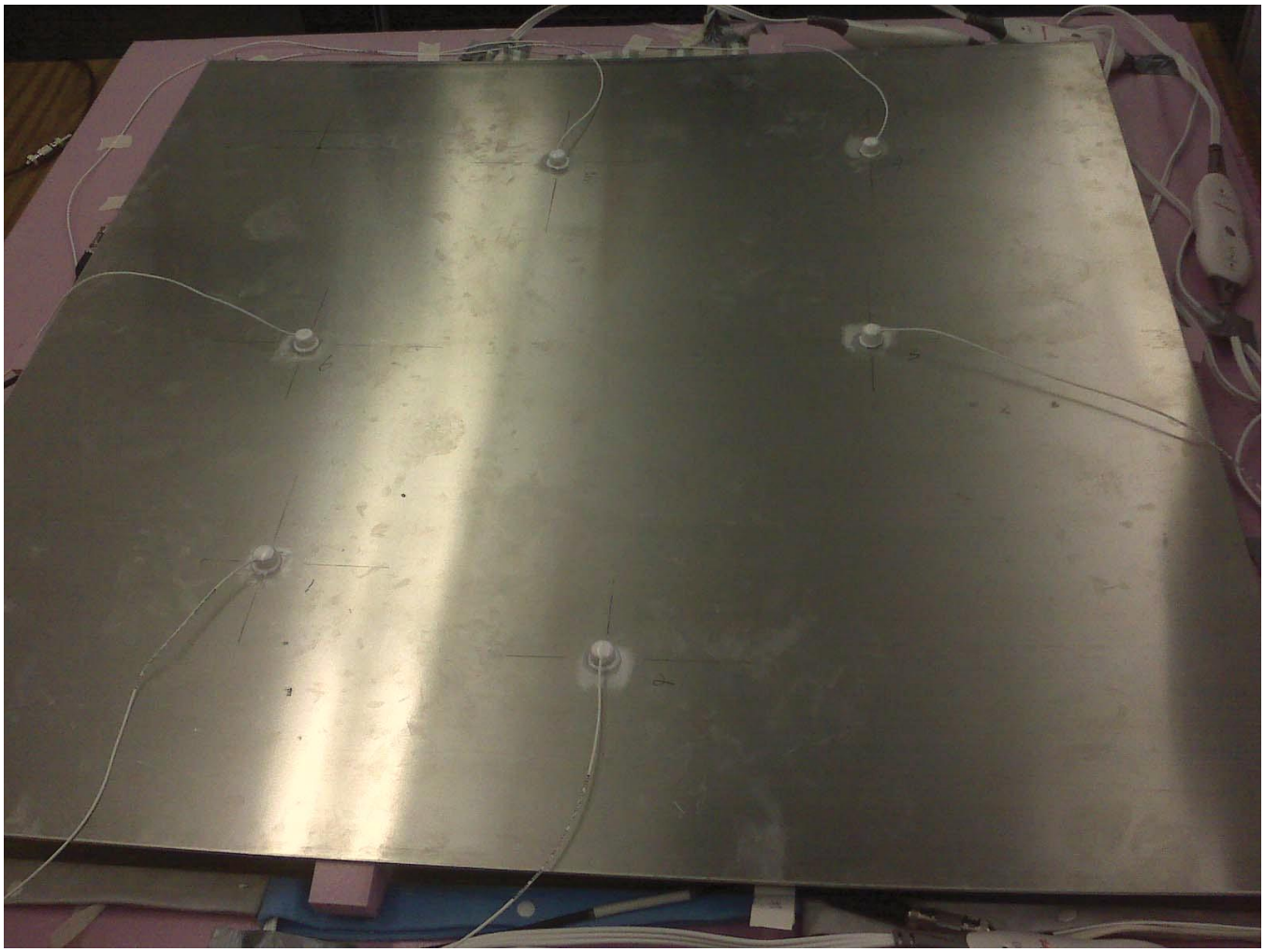

Figure 1B

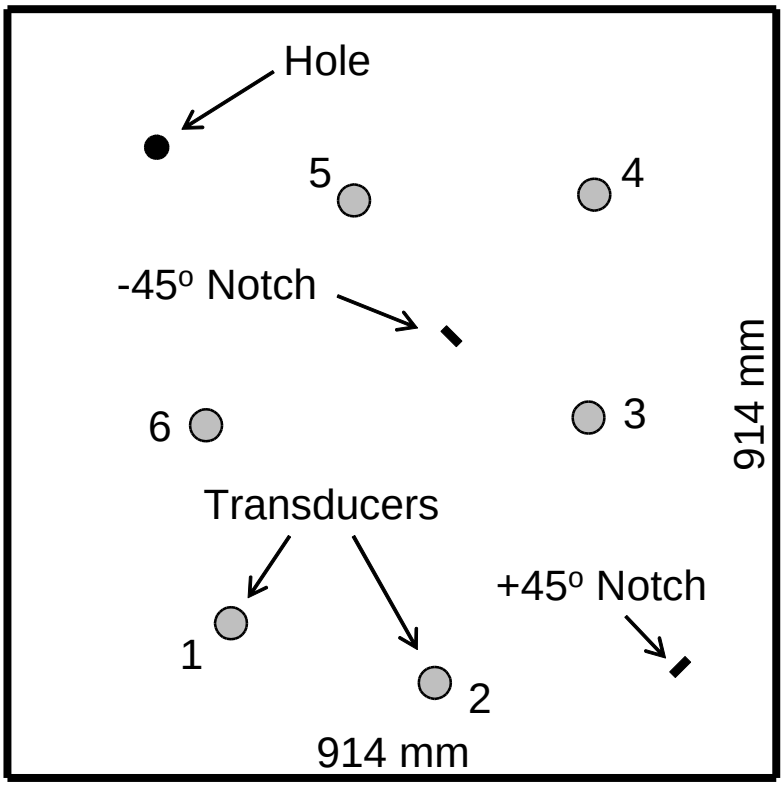

Figure 2

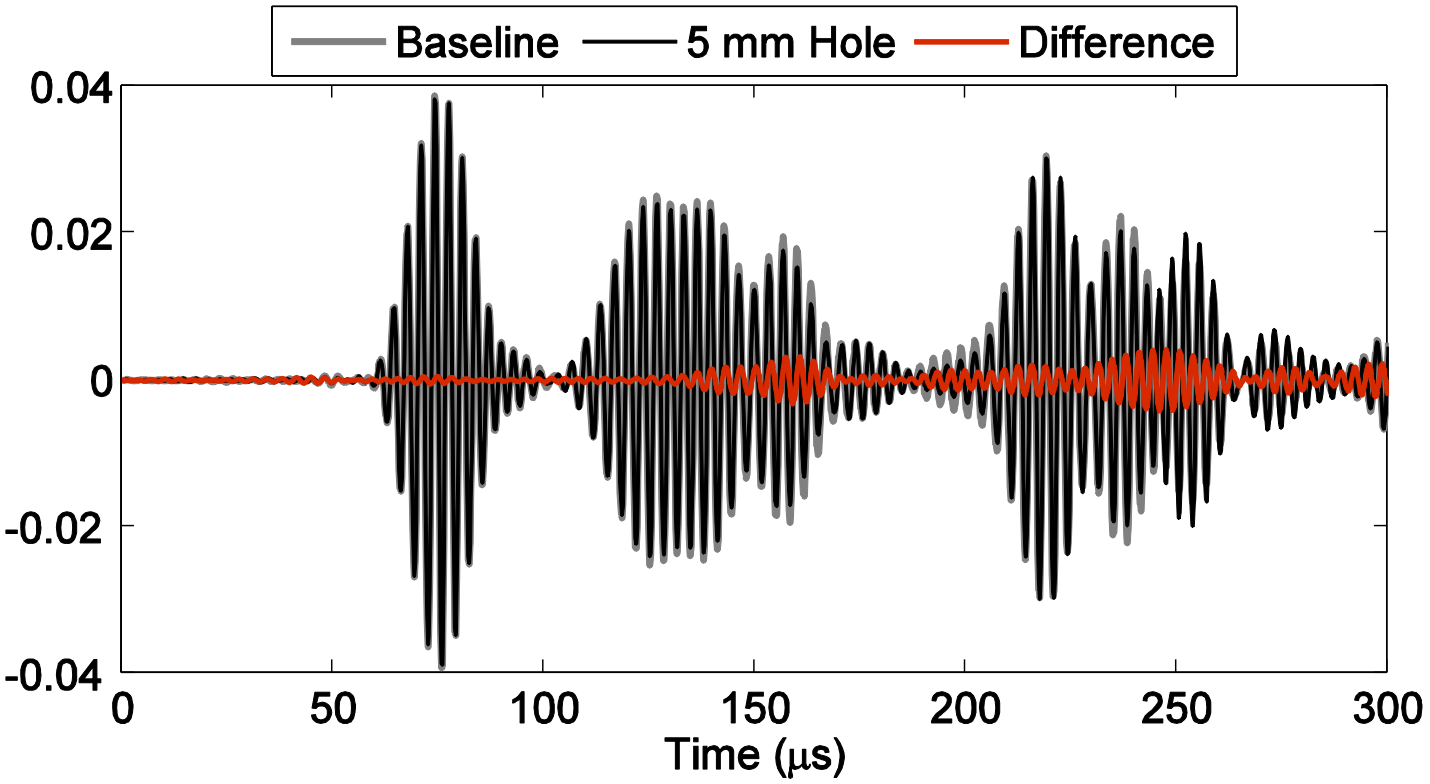
Baseline
5 mm Hole
Difference
0.04
0.02
0
-0.02
-0.04
0
50
100
150
200
250
300
Time (μs)

Figure 3A

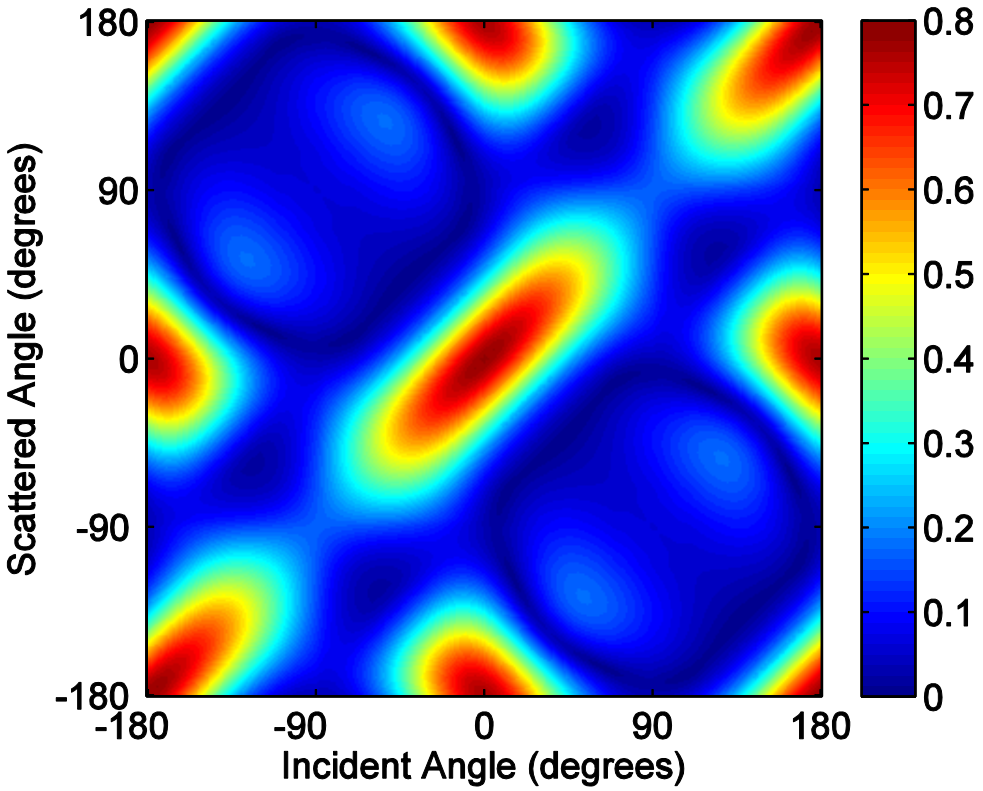
180
90
0
-90
-180
Scattered Angle (degrees)
-180
-90
0
90
180
Incident Angle (degrees)
0.8
0.7
0.6
0.5
0.4
0.3
0.2
0.1
0

Figure 3B

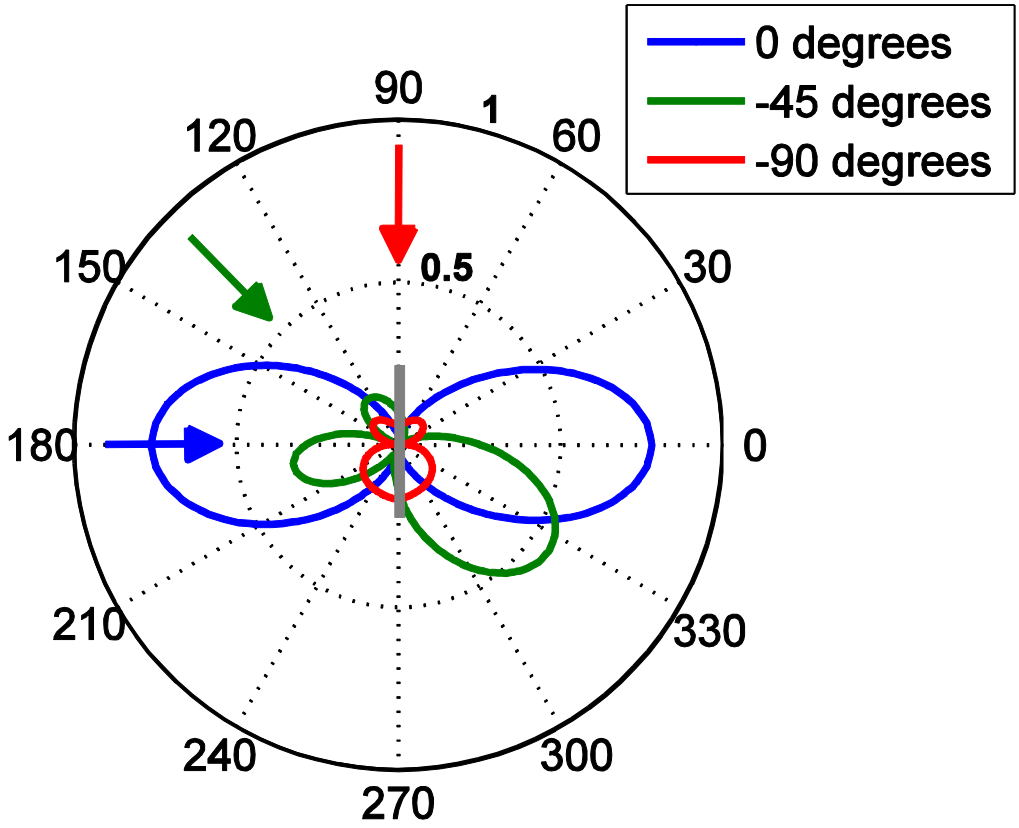
0 degrees
-45 degrees
-90 degrees
90
1
60
120
150
0.5
30
180
0
210
330
240
300
270

Figure 4

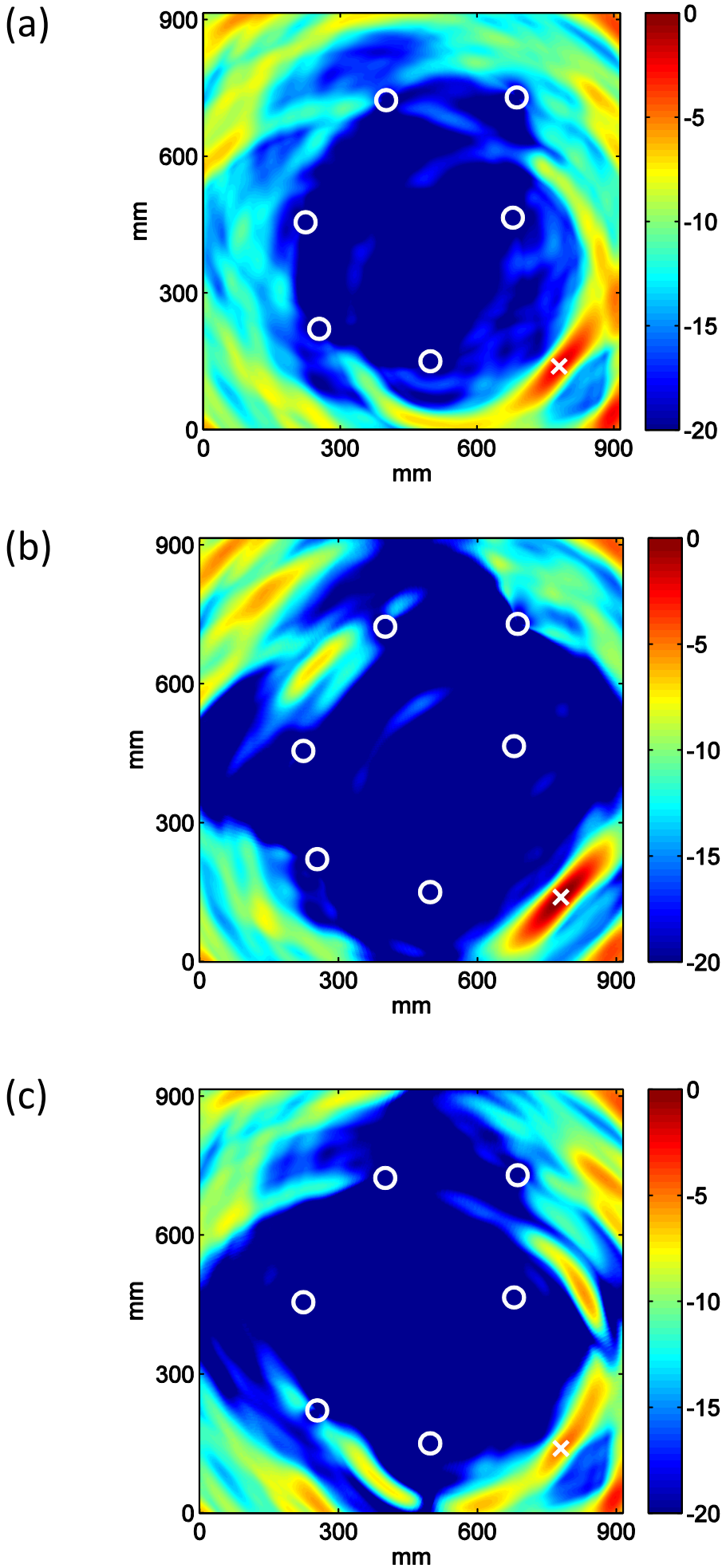
(a)
900
600
300
0
mm
0
300
600
900
mm
0
-5
-10
-15
-20
(b)
900
600
300
0
mm
0
300
600
900
mm
0
-5
-10
-15
-20
(c)
900
600
300
0
mm
0
300
600
900
mm
0
-5
-10
-15
-20

Figure 5

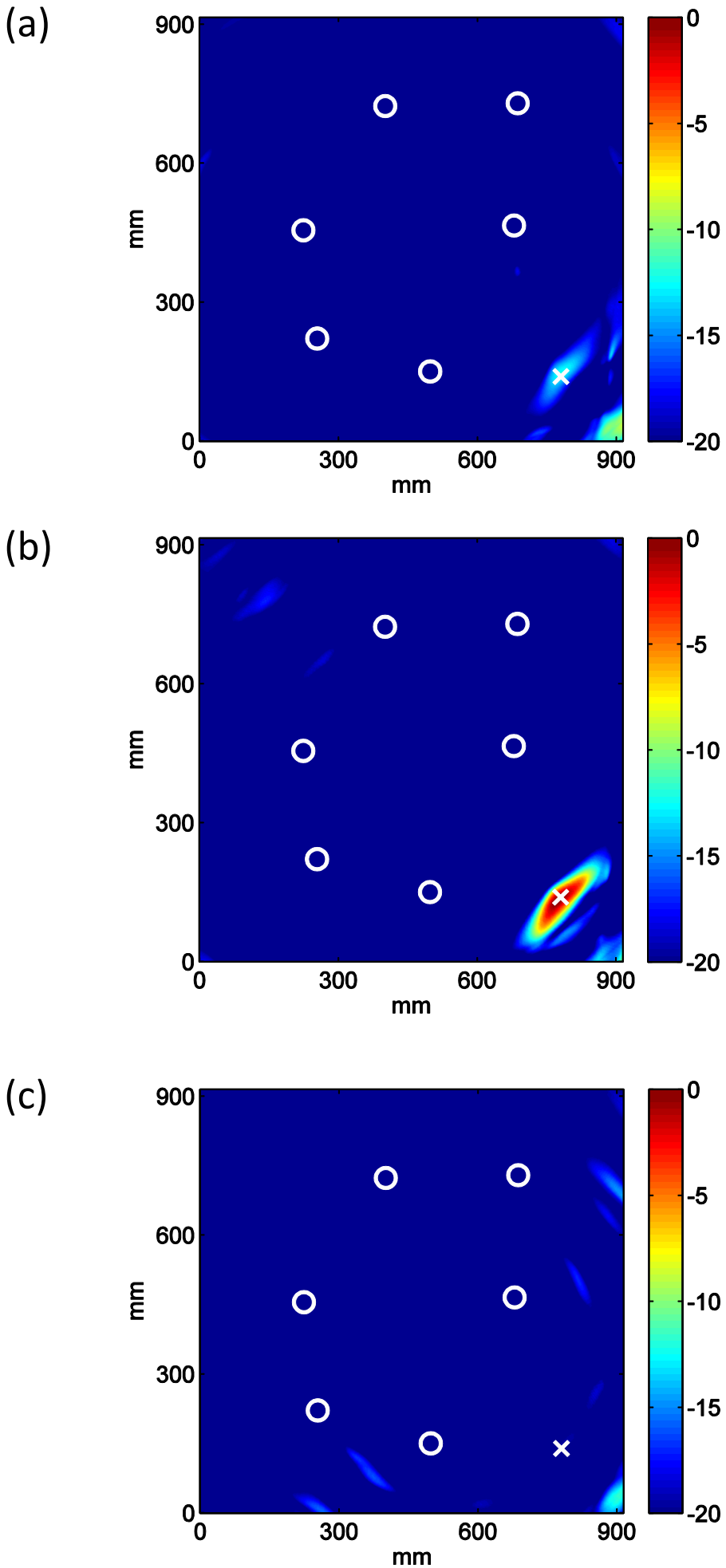

Figure 6

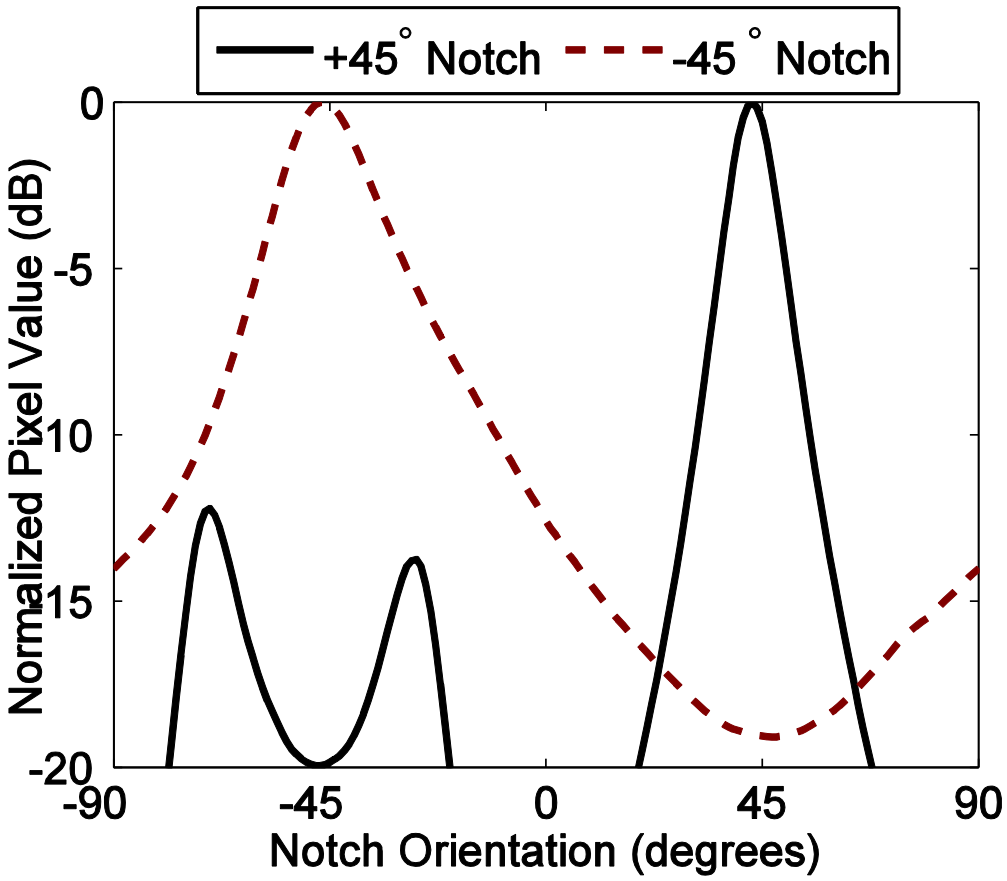
+45° Notch
-45° Notch
Normalized Pixel Value (dB)
0
-5
-10
-15
-20
-90
-45
0
45
90
Notch Orientation (degrees)